Simultaneous Shape Reconstruction and Force Estimation of Soft Bending Actuators Using Distributed Inductive Curvature Sensors

Yu Mei, *Graduate Student Member, IEEE*, Lei Peng, Hongyang Shi, Xinda Qi, *Graduate Student Member, IEEE*, Yiming Deng, *Senior Member, IEEE*, Vaibhav Srivastava, *Senior Member, IEEE*, and Xiaobo Tan, *Fellow, IEEE*

***Abstract*—Soft robots, with their remarkable advantages in various applications, face the critical challenge of embodied perception, encompassing proprioceptive sensing and perceiving unknown environments (exteroception). In this article, we achieve simultaneous continuous shape reconstruction and external force estimation for soft bending actuators using only a proprioceptive curvature sensor. We introduce a novel distributed inductive curvature sensor designed for capturing continuous shape through electromagnetic induction. In addition, we enhance an analytical static model based on the Euler–Bernoulli curved beam theory to predict the shape under pneumatic actuation and external forces. Furthermore, a model-based optimization algorithm is proposed to estimate external forces based on the measured shape. Extensive experimental validation supports the efficacy of the proposed sensor and algorithms.**

***Index Terms*—Curvature sensors, force estimation, inductive coils, shape reconstruction, soft bending actuators.**

I. Introduction

DUE to their intriguing properties, such as intrinsic compliance and safe human–robot interaction, soft robots have been extensively studied in exploring unknown environments [1] and grasping delicate objects [2]. To enable soft robots to possess embodied intelligence, it is significant for them to acquire the embodied perception necessary to obtain essential self-state feedback and perceive unknown environments. However, unlike traditional rigid robots that are typically equipped with reliable sensors, soft robots face challenges in perception due to their infinite degrees of freedom. For example, high-accuracy continuous shape sensing is important for obstacle avoidance and position control, but it is challenging, especially under the influence of gravity and external forces [3]. Moreover, it is crucial for soft robots to estimate external forces without exterior sensors when interacting with the environment in applications such as minimally invasive surgery [4]. Therefore, it is essential to develop a sensory system for soft robots, enabling simultaneous continuous shape sensing and external force estimation.

While advances in modeling have enabled open-loop control for soft robots in limited cases [5], [6], proprioceptive feedback is essential for closed-loop control in the presence of unknown external loads and complex nonlinear behaviors, such as hysteresis and viscoelastic effects [3]. Curvature sensors, crucial for soft robots with prevalent bending motion, have included resistive and piezoresistive bend sensors [7], [8], [9], liquid metal-based sensors [10], and IMU-based sensors [11]. Nevertheless, most studies only address the measurement of single-point curvature, primarily due to the complicated packaging process and sensing techniques [12]. Recent efforts to measure multipoint curvatures focused on distributed sensors and machine learning to establish mapping from sensor signals to full shape deformation [13], [14]. Despite notable shape sensing capabilities, these methods often have complex sensor structures and tightly coupled sensor data that are time-consuming to process. To employ machine learning for shape reconstruction, they frequently require extensive data and significant tuning of neural network parameters. Optical sensors like fiber Bragg grating (FBG) sensors can measure strains at multiple locations and enable shape reconstruction [12]. However, they are limited by high instrumentation costs and temperature dependence. Our shape sensor is inspired by a recent study, known as ShArc, which introduced a low-cost, scalable, and responsive geometric technique for multibend shape sensing through the detection of differential capacitance [15]. However, ShArc lacks high spatial resolution, requiring two receiver pads for the measurement of each sensor segment's curvature.

Intrinsic force sensing refers to the inference of external forces acting on the soft robot without the use of dedicated force

Manuscript received 20 January 2024; revised 25 March 2024; accepted 30 April 2024. Date of publication 21 May 2024; date of current version 16 August 2024. Recommended by Technical Editor G. Berselli and Senior Editor Q. Zou. This work was supported in part by the National Science Foundation under Grant CMMI 1940950 and Grant CNS 2237577. *(Corresponding author: Yu Mei.)*

Yu Mei, Lei Peng, Xinda Qi, Yiming Deng, Vaibhav Srivastava, and Xiaobo Tan are with the Department of Electrical and Computer Engineering, Michigan State University, East Lansing, MI 48823 USA (e-mail: meiyu1@msu.edu; penglei1@msu.edu; qixinda@msu.edu; dengyimi@msu.edu; vaibhav@msu.edu; xbtan@egr.msu.edu).

Hongyang Shi is with the Department of Electrical and Computer Engineering, University of Texas at Austin, Austin, TX 78712 USA (e-mail: hongyangshi@utexas.edu).

This article has supplementary material provided by the authors and color versions of one or more figures available at https://doi.org/10.1109/TMECH.2024.3397825.

Digital Object Identifier 10.1109/TMECH.2024.3397825

sensors [4]. It is typically realized based on some configuration-level information (such as shape measurement) and the actuation input. This kind of exteroception is complicated due to strong coupling between the kinematics and the statics of soft robots [16]. Some past works focused on characterizing the contact forces, for example, estimating the external load using an augmented rigid body model [17], and predicting the contact force through a long short-term memory network [16]. However, most studies cannot achieve both accurate force estimation (magnitude and orientation) and high-resolution shape sensing simultaneously.

In this work, we present, to the best of the authors' knowledge, the first multimodal perception system for soft robots, encompassing not only continuous shape proprioception but also accurate intrinsic force sensing. The most relevant work we can find is a continuum robot with FBG-based torsion sensing [18], which, while capable of estimating both shape and tip force simultaneously, lacks complete proprioception due to the need for an external pose sensor. Our first contribution is designing a novel distributed inductive curvature sensor for real-time monitoring of the shape of soft bending actuators. Compared with previous induction-based proprioceptive sensing approaches that require wrapping an actuator with conductive wires [19], [20], the fabrication of the proposed sensor is easily implementable and scalable for various bending actuators. In addition, a force estimation algorithm is developed to estimate the external forces acting on soft bending actuators by enhancing the Euler–Bernoulli curved beam theory.

The rest of this article is organized as follows. The design and fabrication of the proposed proprioceptive curvature sensors are presented in Section II, followed by the shape reconstruction algorithm based on piecewise-constant curvature (PCC) in Section III. In Section IV, we describe the modeling of soft bending actuators, considering both the presence and absence of external forces, and develop a model-based force estimation algorithm. The experimental results for evaluating the sensor and algorithms are presented in Section V. Finally, Section VI concludes this article and provides future work directions.

II. Distributed Inductive Curvature Sensors

A. Design and Fabrication of the Curvature Sensors

A distributed inductive curvature sensor, shown in Fig. 1, is developed for shape sensing in soft actuators. It measures distributed curvatures by detecting relative shifts between the receiver strip and transmitter strip through electromagnetic induction, where the strips populated with inductive coils are made with the flexible printed circuit board (FPCB) technology. The spacer strips, made of blank FPCBs, are stacked to maintain a specified distance d between the receiver and transmitter strips. The receiver strip, spacer strips (eight used in this work), and the transmitter strip are stacked together from top to bottom and inserted into the silicone sleeve, as shown in Fig. 1(a). The silicone sleeve (Exoflex-0030, Smooth-on) is flexible enough to attach to soft bending actuators without compromising their stiffness. A PVC membrane (Morepack) is attached to the inner surface of the sleeve during its curing process. The membrane tightly encases the strips to prevent loosening in the thickness

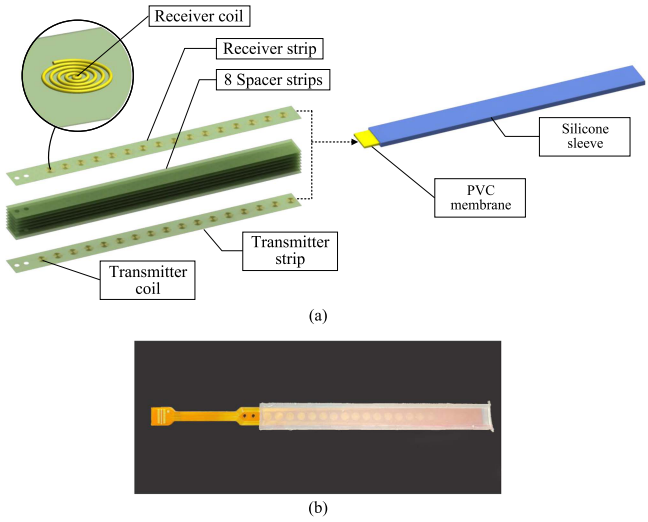

Fig. 1. Illustration of the proposed curvature sensor. (a) Components and assembly layout of the sensor. (b) Assembled prototype.

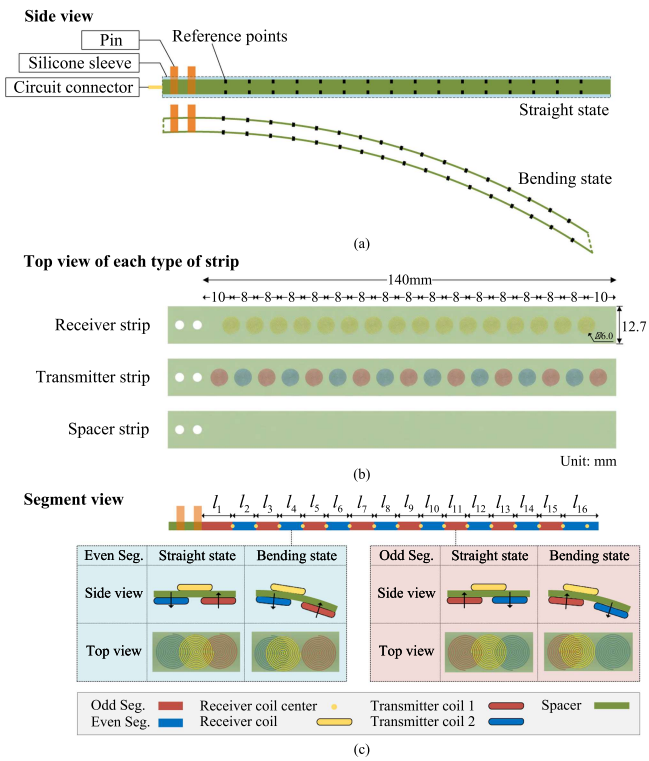

Fig. 2. Design and concept of the distributed inductive curvature sensor. (a) Side view of the sensor with N reference points (top and bottom) along the length, in both straight and bending states. (b) Top view of each strip in the sensor. (c) Illustration of the curvature sensing principle for each segment.

direction and reduce friction between the strips and silicone, allowing for free sliding. Fig. 1(b) depicts the assembled sensor prototype.

To fix the layers, 3-D-printed cylinder pins are passed through the holes of strips on one side, as shown in Fig. 2(a). To discuss the sensor design and sensing principle, consider virtual reference points uniformly spaced on the top and bottom strips along the sensor length, where the corresponding top and bottom

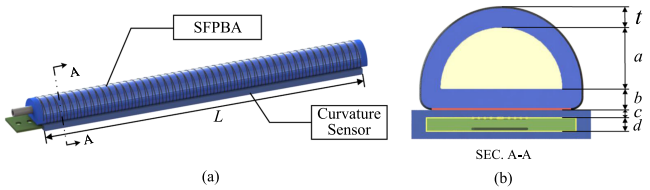

Fig. 3. (a) Illustration of the assembled robot. (b) Cross-sectional view with notation for geometric parameters.

reference points are aligned. Here the number of reference points on each strip corresponds to the number of sensing segments. When the sensor bends into a curved shape, a misalignment occurs between the reference points on the top and bottom strips. The receiver strip has N coils whose centers are aligned with the reference point. In the transmitter strip, $N+1$ transmitter coils are evenly arranged, and the middle points between adjacent transmitter coils are aligned with the reference points, as shown in Fig. 2(b). During operation, a sinusoidal voltage with a constant amplitude is applied to each transmitter coil, generating an alternating current (ac) magnetic field. The ac magnetic fields produced by adjacent transmitter coils have opposite directions, as distinguished by the red and blue coils in Fig. 2(b). With this arrangement, each receiver coil can sense the combined influence of the magnetic fields generated by the underlying transmitter coils, and thus the spatial shift between the receiver coil and the corresponding transmitter coils.

In this work, we focus on the receiver strips' shape since it will be closer to the soft actuator. For analysis, we divide the receiver strip into N segments, with the length of the ith segment denoted as l_i, where $i = 1, 2, \ldots, N$, as shown in Fig. 2(c). Each segment has the center of a receiver coil on its end (toward the free end of the sensor), with the exception of the last segment, where the segment length extends to the tip of the sensor structure. Due to the alternating pattern of transmitter coils, we distinguish "even" and "odd" segments, as shown in Fig. 2(c), where one can see the relationships between sensed differential magnetic fields and receiver–transmitter spatial shifts for even and odd segments, respectively. Using the signals detected from each segment along the sensor, one can extract the relative shifts and distributed curvatures using the algorithm detailed in Section III.

B. Integration With Soft Bending Actuator

While there are various ways to implement soft bending actuators, we employ a soft fiber-reinforced pneumatic bending actuator (SFPBA) as an example. The SFPBA is fabricated by casting silicone (Dragon Skin 20, Smooth-On), as described in [5]. The top surface of the sensor is attached to the bottom surface of SFPBA using silicone glue (SIL-Poxy, Smooth-On), as shown in Fig. 3(a), forming a soft bending actuator with proprioceptive curvature sensing.

III. Shape Reconstruction Algorithm

A shape reconstruction algorithm for the proposed curvature sensor is developed. The signal values of N receiver coils represent the amplitudes of their induced ac voltages, and are

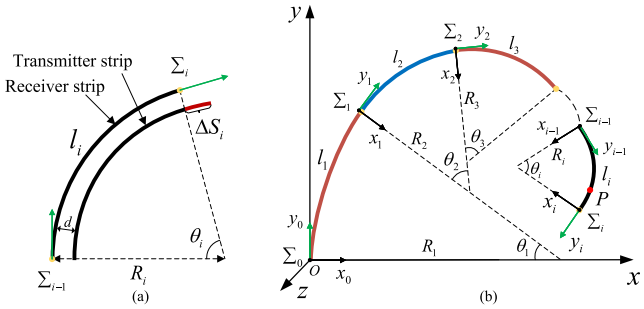

Fig. 4. Illustration of geometric relationship for shape reconstruction. (a) Relationship between the relative shift ΔS_i and the bending geometry in the ith segment. (b) PCC kinematic representation for the entire receiver strip.

denoted as $A \in \mathbb{R}^N$. As mentioned before, these signals are determined by the receiver–transmitter spatial shifts $S \in \mathbb{R}^N$. The obtained signals from the measurement hardware have a constant offset $A_0 \in \mathbb{R}^N$. We consider ΔA, with the offset removed, in the reconstruction process as follows:

$$\Delta A = A - A_0 \tag{1}$$

where the offset A_0 is obtained as the sensor signals when the sensor is flat. Due to the opposite direction of sensed differential magnetic fields, the relationships between the components of ΔA and the corresponding spatial shifts in odd and even segments exhibit opposite monotonic trends. Therefore, we use separate polynomial functions, f_{odd} and f_{even}, to describe them; in particular, for segment i as follows:

$$S_i = \begin{cases} f_{\text{odd}}(\Delta A_i) = \sum_{k=0}^{n} a_k (\Delta A_i)^k, & i \text{ is odd} \\ f_{\text{even}}(\Delta A_i) = \sum_{k=0}^{n} b_k (\Delta A_i)^k, & i \text{ is even} \end{cases} \tag{2}$$

for $n \geq 1$, where S_i is the total relative shift of the reference point in the ith segment, a_k and b_k $(k = 1, \ldots, n)$ are coefficients of the polynomial functions in odd and even segments, respectively. These coefficients are identified by experiments.

After obtaining the total relative shift S_i, one can calculate the curvatures of different segments through geometry. First, the *local* relative shift ΔS_i in the ith segment can be computed as the difference between the total relative shifts in the $(i-1)$th and ith segment as follows:

$$\begin{cases} \Delta S_i = S_i - S_{i-1}, & i = 2, 3, \ldots, N \\ \Delta S_1 = S_1. \end{cases} \tag{3}$$

The continuous shape of the sensor with N segments can be approximated by a set of arcs with constant curvatures, widely known as the PCC model [21]. With the PCC model, the local relative shift ΔS_i in the ith segment [see Fig. 4(a)] is related to the constant curvature κ_i of the ith segment as follows:

$$\kappa_i = \frac{\Delta S_i}{d l_i} \tag{4}$$

where d is the distance between the two strips. Note that κ_i can be negative when ΔS_i is negative.

The PCC kinematic representation for the sequential segments of the entire receiver strip of the sensor is shown in Fig. 4(b). For the ith segment, it has the length l_i, the curvature κ_i, and the

bending angle θ_i. A coordinate frame Σ_i is attached at the tip of the ith segment, whereas an inertial frame Σ_0 is located at the origin. For each coordinate frame Σ_i, its x-axis points toward the center of the arc, its y-axis is aligned with the tangential direction, and the z-axis is defined according to the right hand rule. The homogeneous transformation matrix mapping from Σ_{i-1} to Σ_i can be formulated as follows:

$$T_i^{i-1}(\theta_i) = \begin{bmatrix} R_z(-\theta_i) & p_i^{i-1}(\theta_i) \\ 0 & 1 \end{bmatrix}$$

$$\text{where} \quad p_i^{i-1}(\theta_i) = \begin{bmatrix} \frac{l_i}{\theta_i}(1-\cos(\theta_i)) & \frac{l_i}{\theta_i}\sin(\theta_i) & 0 \end{bmatrix}^T$$

$$\theta_i = l_i \kappa_i \tag{5}$$

$R_z(\theta) \in SO(3)$ indicates a rotation about the z-axis by the angle θ and $p_i^{i-1}(\theta_i)$ represents the position of the ith segment's tip with respect to the local base frame Σ_{i-1}. If a point P with arc length s is in the ith segment, as shown in Fig. 4(b), then the coordinates of P with respect to the inertial frame Σ_0, denoted as $p^0(s)$, can be computed as follows:

$$\begin{bmatrix} p^0(s) \\ 1 \end{bmatrix} = T_1^0(\theta_1) \cdot T_2^1(\theta_2) \cdots T_{i-1}^{i-2}(\theta_{i-1}) \cdot \begin{bmatrix} p^{i-1}(s) \\ 1 \end{bmatrix} \tag{6}$$

where $p^{i-1}(s)$ is the position of P with respect to Σ_{i-1}, which can be computed as follows:

$$p^{i-1}(s) = \begin{bmatrix} \frac{l_i}{\theta_i}\left(1-\cos(\theta_i \frac{s-L_{i-1}}{l_i})\right) & \frac{l_i}{\theta_i}\sin(\theta_i \frac{s-L_{i-1}}{l_i}) & 0 \end{bmatrix}^T$$

$$s \in (L_{i-1}, L_i] \tag{7}$$

where L_i is the sum of the length of the first i segments. Note that L_0 is defined as 0, and L_N equals the actuator length L.

In summary, given the signal values of A, the position $p^0(s)$ of every point on the sensor can be determined.

IV. Model-Based Force Estimation Algorithm

A. Static Modeling in the Absence of External Forces

As the air pressure in the chamber increases, the SFPBA integrated with the curvature sensor bends in an arc with a constant curvature K_0 when there are no external forces and the weight of the actuator is negligible [5]. Based on the static modeling of SFPBA as discussed in [8], the relationship between the internal air pressure P_{in} and the bending angle θ_0 can be obtained from the moment balance equation as follows:

$$M_a = M_{\theta_0} + M_s. \tag{8}$$

Here M_a represents the pressure-induced bending moment, M_{θ_0} is the bending moment caused by the elasticity of SFPBA, and M_s represents the bending moment required to bend the sensor layer. M_a can be written as follows:

$$M_a = \frac{4a^3 + 3\pi a^2 b}{6} P_{\text{in}} \tag{9}$$

where a is the inner radius of SFPBA's chamber, and b is the bottom layer thickness, as shown in Fig. 3(b). M_{θ_0} can be formulated in terms of θ_0 as follows:

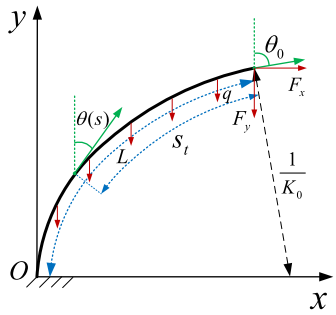

Fig. 5. Force analysis diagram under gravity and external force at the tip.

$$M_{\theta_0} = \int_0^b s_\beta \cdot 2(a+t)\beta \mathrm{d}\beta + 2\int_0^t \left(\int_0^{\frac{\pi}{2}} s_{\tau,\phi} \left((a+\tau)^2 \sin\phi + b(a+\tau) \right) \mathrm{d}\phi \right) \mathrm{d}\tau \tag{10}$$

$$\text{where } s_\beta = \bar{\mu}\left(\lambda_\beta - \frac{1}{{\lambda_\beta}^3}\right), \lambda_\beta = \frac{\beta\theta_0}{L} + 1$$

$$s_{\tau,\phi} = \bar{\mu}\left(\lambda_{\tau,\phi} - \frac{1}{{\lambda_{\tau,\phi}}^3}\right), \lambda_{\tau,\phi} = \frac{R + b + \sin\phi(a+\tau)}{R} \tag{11}$$

where t is the wall thickness, (s_β, λ_β) and $(s_{\tau,\phi}, \lambda_{\tau,\phi})$ are the longitudinal stress and stretch of the flat rectangular wall and the hemicylindrical top wall, respectively, and R is the radius of the circular arc. $\bar{\mu}$ represents the effective shear modulus, determined through calibration. M_s can be approximated as a linear function of θ_0 [8] as follows:

$$M_s = \mu_s \theta_0 \tag{12}$$

where μ_s is the bending stiffness of the sensor determined by calibration.

By substituting (9)–(12) into (8), we can numerically solve for the bending angle θ_0 with a given input pressure P_{in}, and the curvature K_0 is obtained by $K_0 = \theta_0 / L$.

B. Static Modeling With External Forces

With gravity and external forces, the actuator will not maintain a shape with constant curvature, so the static modeling should consider these forces, including the effects of the actuation pressure, a point force, and a distributed force (gravity). Without the loss of generality, assume that the point force is applied at the tip, which commonly occurs when the actuator presses against or grabs an external object [8], [22]. The tip force can be decomposed into horizontal force F_x and vertical force F_y, as shown in Fig. 5. In addition, the gravity is a uniformly distributed force applied along the length, and the gravity q of each length unit can be calculated as $q = mg/L$, where m is the total weight of the robot including the SFPBA and the sensor layer, and g is the gravitational acceleration.

As discussed in [22] and [23], the large deflection of the soft actuator can be modeled using the Euler–Bernoulli beam theory adapted for a curved cantilever beam. The shape of the actuator can be obtained by solving the following ordinary differential equation (ODE):

$$EI\left(\frac{\mathrm{d}^2(\theta(s_t))}{\mathrm{d}{s_t}^2}\right) + F_x\cos(\theta(s_t)) + F_y\sin(\theta(s_t)) + qs_t\sin(\theta(s_t)) = 0 \tag{13}$$

where s_t is the arc length measured from the tip ($s_t \in [0, L]$ and $s_t = L - s$), and $\theta(s_t)$ denotes the angle between the y-axis and the tangential axis of the beam at s_t, as illustrated in Fig. 5. E represents the equivalent Young's modulus, and I is the second moment of area. EI is referred to as a single parameter describing the flexural rigidity. The boundary conditions for the above ODE include the following:

$$\theta(L) = 0, \qquad \frac{\mathrm{d}\theta(0)}{\mathrm{d}s_t} = -K_0 \tag{14}$$

where the initial curvature K_0 is determined by static modeling for free motion with a given pressure P_{in} (see Section IV-A).

The flexural rigidity EI in the above static modeling is usually considered to be constant, thus the previous studies utilize a few pairs of pressures and loads to determine EI [22], [23]. However, the flexural rigidity of soft pneumatic robots typically increases in proportion to higher actuation pressure [24], [25]. Therefore, we introduce a stiffness-tunable model, expressing the relationship between flexural rigidity EI and actuation pressure P_{in} as a linear function:

$$EI(P_{\text{in}}) = \gamma_0 + \gamma_1 P_{\text{in}} \tag{15}$$

where γ_0 and γ_1 are experimentally determined coefficients. Substituting (15) into (13) yields the following ODE:

$$EI(P_{\text{in}})\left(\frac{\mathrm{d}^2(\theta(s_t))}{\mathrm{d}{s_t}^2}\right) + F_x\cos(\theta(s_t)) + F_y\sin(\theta(s_t)) + qs_t\sin(\theta(s_t)) = 0. \tag{16}$$

After solving $\theta(s_t)$ in (16) using the shooting method, we integrate to obtain the coordinates of every point $p(s_t)$:

$$\begin{cases} x(s_t) = \int_L^{s_t}\sin(\theta(\tau))\mathrm{d}\tau \\ y(s_t) = \int_L^{s_t}\cos(\theta(\tau))\mathrm{d}\tau \\ p(s_t) = \begin{bmatrix} x(s_t) & y(s_t) & 0 \end{bmatrix}^T. \end{cases} \tag{17}$$

C. Force Estimation Algorithm

Utilizing sensor signals and actuation pressure as inputs, we propose an estimation algorithm for the external force applied on the robot, as depicted in Fig. 6. As discussed in Section III, the coordinates of every point along the robot $p^0(s)$ can be reconstructed with given A and A_0, where $s \in [0, L]$. With given P_{in}, the initial curvature K_0 can be calculated through static modeling without external forces, and the flexural rigidity is determined by the stiffness-tunable model in (15). Now with any given horizontal force F_x and vertical force F_y, the robot's configuration $p(s_t)$ can be predicted using (13)–(17). The external forces $(\hat{F}_x, \hat{F}_y)$ can be estimated by minimizing

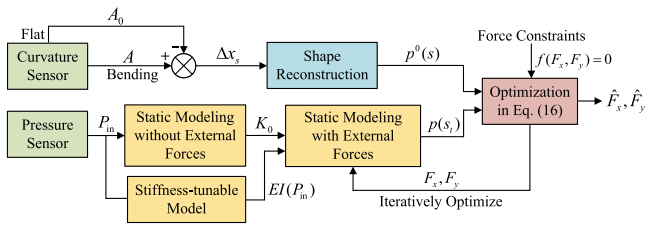

Fig. 6. Schematic of the proposed force estimation algorithm. In this framework, the inputs consist of the signal values A and the background signal values A_{bg} from the curvature sensor, along with the actuation pressure P_{in} from a pressure sensor. The outputs are optimal force $\hat{F}_x, \hat{F}_y$ making the predicted shape $p(s_t)$ closest to the reconstructed shape $p^0(s)$.

the difference between the predicted shape $p(s_t)$ and the reconstructed shape $p^0(s)$. Furthermore, constraints on F_x and F_y for practical applications, such as fixed directions in inertial or body coordinates [22], can be incorporated in the estimation process. In summary, this can be formulated as a least-square optimization problem:

$$(\hat{F}_x, \hat{F}_y) = \underset{F_x, F_y}{\arg\min} \int_0^L \left(\left\|p^0(s) - p(s_t)\right\|\right)^2 \mathrm{d}s \quad \text{s.t.} \quad f(F_x, F_y) = 0 \tag{18}$$

where $s_t = L - s$, and the function f captures the constraints on F_x and F_y.

V. Experimental Results

A. Experimental Setup

To validate the proposed curvature sensor and force estimation framework, an experimental platform is developed, as shown in Fig. 7(a). The SFPBA, weighing 25.86 g with structural dimensions $(a, b, t, L) = (6.35, 2, 2, 134)$ mm, is clamped at the proximal end to the horizontal framing rail, and the distal end is free to bend and interact with objects. A pneumatic control board is utilized to control the air pressure P_{in} via an underlying PID controller.

The sensor weighs 13.41 g, making the total robot weight be 39.27 g. The silicone sleeve thickness c is 0.75 mm, and the distance d between the top and bottom strips is 1 mm. The receiver strip is segmented into 16 sections (N=16) with lengths $(l_1, l_2, l_3, \ldots, l_{15}, l_{16}) = (10, 8, 8, \ldots, 8, 10)$ mm, as illustrated in Fig. 2(b). Both receiver and transmitter coils, each with 6 mm diameters and a total of 20 turns, are arranged in two FPCB layers. The spacing between coils is 8 mm. The hardware system for the curvature sensor includes a power supply, a waveform generator, and a circuit board operating on a ±5 V power supply (KETHELEY 1103). A signal generator provides the excitation voltage for the transmitter coil array, applying a 1 MHz sinusoidal signal with a 2 V amplitude. Using the designed circuit board, the 16 receiver coil signals are sequentially processed via a multiplexer chip (ADG1406). The selected signal is processed by a lock-in amplifier (AD8333) to capture the induced ac voltage's amplitude and is then converted into a digital signal using the embedded ADC in the MCU (STM32F407).

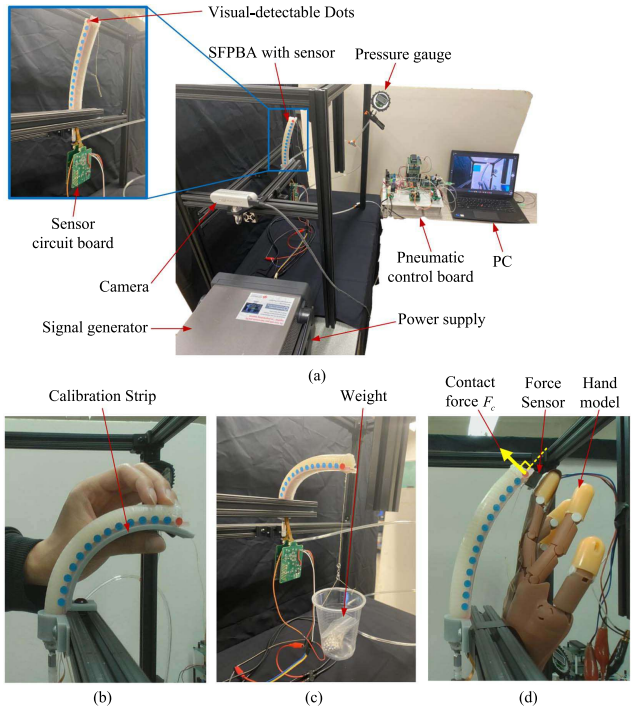

Fig. 7. Illustration of the experimental setup and processes. (a) Overall configuration for the SFPBA with the curvature sensor. (b) Calibration process for shape reconstruction by pressing the robot against the calibration strip. (c) Validation experiment for static modeling with external force by hanging a load on the tip. (d) Validation experiment for the force estimation algorithm with applied contact force F_c on the fingertip of a hand model.

To capture the actual shape of the robot (as ground truth), a high-resolution camera (RealSense D435, Intel) is mounted on the side, as depicted in Fig. 7(a). Fourteen color dots, uniformly distributed along the actuator's bottom layer, capture the shape of that layer, whose length remains unchanged during actuation due to the strain-limiting material [5]. Each dot is detected by analyzing RGB channel mean intensity using MATLAB's *Image Processing Toolbox*.

B. Results on Shape Reconstruction for the Curvature Sensor

To establish the magnitude-shift mapping in (2), various 3-D-printed arc calibration strips with different curvatures are used. Considering the accessible workspace with respect to the length, the radii of calibration strips, R_{cal}, are set to 40, 50, 60, 70, 80, 90, 100, 200, 300, and 400 mm. The corresponding curvatures, κ_{cal}, are determined as 25, 20, 16.67, 14.29, 12.5, 11.11, 10, 5, 3.33, and 2.50 m^{-1}. After mounting each calibration strip, we can manually press the soft actuator onto the calibration strip and collect the signal data, as shown in Fig. 7(b). The actual total relative shift S_i can be determined as $S_i = \kappa_{\text{cal}} \cdot d \cdot L_i$. Afterward, odd and even segment data are curve-fitted in MATLAB to identify coefficients a_k and b_k in (2). We tested the calibrated coefficients using validation strips with untested radii ($R_{\text{val}} = 45$–150 mm). With the proposed shape reconstruction algorithm, the reconstructed shape $p^0(s)$ is obtained for each validation curvature.

TABLE I
COMPARISON OF CONSTRUCTED RESULTS FOR DIFFERENT CURVATURES

	R^*_{val} (mm)	45.75	55.75	65.75	75.75	85.75	95.75	150.75	All
	κ_{val} (m^{-1})	21.86	17.94	15.21	13.20	11.66	10.44	6.63	
$n=1$	κ_{recon} (m^{-1})	21.65	17.60	14.99	12.98	11.50	10.20	6.74	-
	$\delta\kappa$ (%)	0.94	1.88	1.43	1.71	1.39	2.29	1.63	1.61 ± 0.42
	$(\delta p)_{\max}$ (%)	3.98	2.61	1.67	1.42	1.77	2.62	1.21	2.19 ± 0.96
$n=2$	κ_{recon}	21.77	17.73	15.11	13.07	11.58	10.26	6.69	-
	$\delta\kappa$ (%)	0.38	1.13	0.65	0.99	0.74	1.80	0.87	0.94 ± 0.45
	$(\delta p)_{\max}$ (%)	3.66	2.65	1.85	1.24	1.19	2.10	0.98	1.95 ± 0.95
$n=3$	κ_{recon}	21.69	17.75	15.20	13.20	11.71	10.40	6.74	-
	$\delta\kappa$ (%)	0.76	1.04	0.08	0.08	0.46	0.41	1.69	0.65 ± 0.58
	$(\delta p)_{\max}$ (%)	3.01	2.05	1.50	1.22	1.19	1.27	0.89	1.59 ± 0.72

* indicates the actual radii R_{val} considered the silicone sleeve thickness c.
Red numbers represent the best results among $n = 1, 2, 3$.

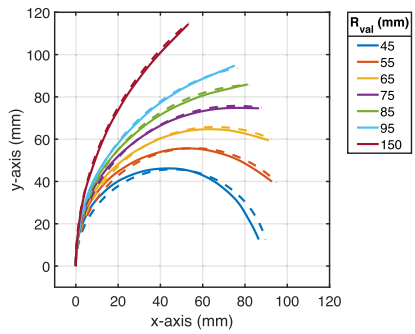

Fig. 8. Shape reconstruction using third-order polynomials on validation strips. The solid and dotted lines represent reconstructed and actual shapes, respectively.

Table I shows the comparison between the actual curvatures κ_{val} and the reconstructed curvatures κ_{recon} for different polynomial degrees ($n = 1, 2, 3$). The reconstructed curvatures κ_{recon} are determined by matching the reconstructed shape $p^0(s)$ with the predicted one via the following least-squares optimization:

$$\begin{cases} \kappa_{\text{recon}} = \arg\min_{\kappa} \int_0^L \left(\left\|p^0(s) - p_{\text{con}}(s,\kappa)\right\|\right)^2 \mathrm{d}s \\ p_{\text{con}}(s,\kappa) = \left[\frac{1}{\kappa}(1-\cos(\kappa s)) \;\; \frac{1}{\kappa}\sin(\kappa s) \;\; 0\right]^T \end{cases} \tag{19}$$

where $p_{\text{con}}(s,\kappa)$ represents the positions of the constructed circular shape with curvature κ along the arc length. While the low relative error $\delta\kappa = |\kappa_{\text{recon}} - \kappa_{\text{val}}|/\kappa_{\text{val}}$ in the curvature measurement confirms the functionality of the proposed sensor, accurate prediction of the position is crucial in the subsequent force estimation framework. We can find the maximum position error $(\delta p)_{\max}$ between the reconstructed shape $p^0(s)$ and the actual validation shape $p_{\text{con}}(s,\kappa_{\text{val}})$ along the arc length with respect to the robot's length as follows:

$$(\delta p)_{\max} = \max_{0 \le s \le L} \left(\frac{\left\|p^0(s) - p_{\text{con}}(s,\kappa_{\text{val}})\right\|}{L} \right) \cdot 100. \tag{20}$$

As shown in Table I, all reconstructed curvature errors are below 2%, and all maximum position errors are under 4%. For $n = 3$, the magnitude-shift mapping achieves the highest accuracy in curvature ($0.65\% \pm 0.58\%$) and position ($1.59\% \pm 0.72\%$). Fig. 8 shows the shape reconstruction results of validation strips with $n = 3$ calibrated coefficients. Compared with ShArc [15], the proposed inductive curvature sensor performs slightly better in reconstructing shapes with small curvature, as it is more sensitive to detect the differential inductance than differential

capacitance within small displacement. However, curvature and position errors increase with larger curvatures, possibly due to unbalanced calibration data—total relative shift S_i. As S_i sums up from 0 for each calibration strip, it includes more small shift data. Another potential factor is the curved deformation of coils during large bending motions, leading to complex changes in magnetic fields and sensing, which may not be accurately captured by sensor calibration. Future research can explore calibration improvement. The proposed inductive curvature sensor, with its compact alternating structure, theoretically has twice as many PCC segments as ShArc within the same length, indicating potential for higher resolution in capturing irregular shapes. Additional experiments also confirm the sensor's immunity to the presence of metallic objects nearby and external dc magnetic fields. Technically, its performance is only impacted by external ac magnetic fields matching the excitation current frequency (1 MHz in this work). Regarding computational efficiency, this shape reconstruction can be implemented in real-time at a frequency of at least 35 Hz on a laptop with an Intel i7-11800H processor and 32.0 GB RAM, as demonstrated in the online video.[1] We note that the inductive sensors have a sensing bandwidth of over 50 kHz. The slowdown is mainly due to the configuration and computation of the circuit board, which can be significantly improved by optimizing embedded processing in the future.

C. Results on Static Modeling

To establish the connection between the air pressure and the bending angle in the absence of external force, we need to calibrate the material properties $\bar{\mu}$ and μ_s. Using the same calibration method in [5], effective shear modulus $\bar{\mu}$ for the SFPBA without the sensor can be identified. The stiffness of sensor μ_s is determined using the calibration procedure in [8]. Notably, an initial bending angle should be added to the analytical bending angle due to the prebending phenomenon.

To validate static modeling with external forces, experiments are conducted with different actuation pressures and tip loads, as shown in Fig. 7(c). The robot is only subject to vertical downward force F_y. We collect a dataset for evaluating the modeling accuracy across the accessible workspace. The dataset includes actual shapes captured from the camera and sensor signals at the steady state after actuation with various pressures, ranging from 20 to 120 kPa in 10 kPa increments. Meantime, tip loads increase progressively from 0 to 0.3 N in 0.1 N steps for each pressure level. The force range is selected to generate comparable moments relative to the actuation moment and to prevent actuator buckling. Effective flexural rigidity EI in (13) is determined for various pressure levels using randomly chosen pressure-load combinations, following the calibration process in [23]. Employing linear regression, we identify the coefficients in (15) as $\gamma_0 = 2.53 \times 10^{-3}$ and $\gamma_1 = 1.25 \times 10^{-5}$. Predicting the shape using (15)–(17) with known P_{in} and F_y, we evaluate the maximum position errors based on the position of 14 colored dots captured by the camera. The averaged maximum position errors between the predicted shape based on analytical modeling and the experimental data are below 6% across different pressures, as shown in Fig. 9(a). At the same time, the sensor measurement errors are below 6.32%. Fig. 9(b) illustrates examples of reconstructed shapes under 40 kPa pressure with various loads, showing consistent patterns observed at other pressure levels. Both sensor measurements and analytical modeling fit the experimental data well, except for the 0.3 N case, which exhibits nonnegligible deviations. The possible reason is that the cross-section of the actuator deforms when the bending is larger, leading to a deviation in the base orientation from the straight upward direction. This factor was not considered in either the sensor-based reconstruction and the analytical model. The overall accuracy of both the analytical model and the sensor allows for directly estimating the external force from the curvature sensor measurement while simultaneously reconstructing the shape.

[1][Online]. Available: https://youtu.be/0Kpc-y5kq6U

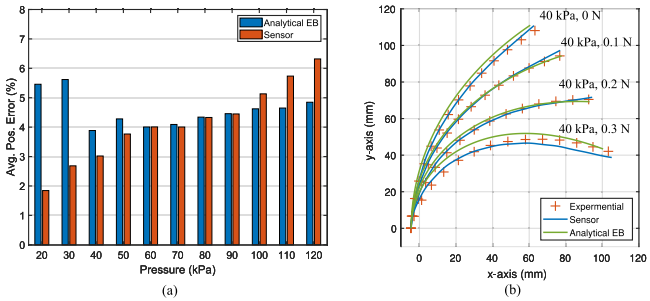

Fig. 9. Experimental results on static modeling. (a) Maximum position errors in shape reconstruction based on analytical Euler–Bernoulli beam theory and sensor measurements, averaged across tip loads at the same pressure level. (b) Comparison of the predicted shapes based on analytical modeling and on the sensor measurement with the ground truth, under 40 kPa pressure with various loads.

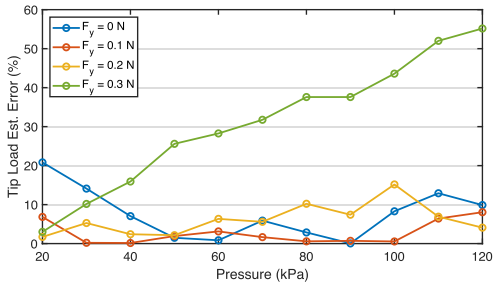

Fig. 10. Force estimation errors for various tip loads F_y under different actuation pressures P_{in}.

D. Results on Force Estimation

Experiments have been conducted to validate the force estimation algorithm in different scenarios.

1) Tip Load Estimation: We utilize the acquired dataset for experiments on tip load estimation, covering various pressure-load combinations. In this scenario, the constraint in (18) stipulates that $F_x = 0$. The tip load F_y is estimated based on the provided actuation pressure and the measured shape based on the curvature sensor, following the framework in Fig. 6.

TABLE II
COMPARISON OF MEAN ERRORS (%) IN CONTACT FORCE ESTIMATION WITH AND WITHOUT GEOMETRIC CONSTRAINT

	Without Constraint			With Constraint		
Force Range (N)	$\hat{F}_x$	$\hat{F}_y$	$\hat{F}_c$	$\hat{F}_x$	$\hat{F}_y$	$\hat{F}_c$
0–0.1	4.13	2.93	4.27	1.57	3.91	2.61
0.1–0.2	8.13	2.51	4.40	3.02	3.43	1.35
0.2–0.3	17.70	13.18	9.04	7.42	4.29	7.52
0.3–0.4	6.29	42.95	12.19	9.15	21.01	8.17
Mean of Full Range	14.90	12.91	7.21	5.15	6.77	4.86

Fig. 10 shows the force estimation error for each pressure-load combination. The average estimation error is $11.9\% \pm 14.4\%$ with respect to the maximum load (0.3 N). While the tip load estimation error is significant when the load is 0.3 N, the force estimation error when the load is 0–0.2 N is only $5.49\% \pm 4.99\%$. The main reason is that both sensor measurement and analytical static modeling have larger errors when the bending is significant, causing the estimated force $\hat{F}_y$ to be optimized to approach the deviated shape in (18).

2) Contact Force Estimation: The contact force is a type of follower force, wherein the tip force maintains a fixed direction in body coordinates. In this scenario, the robot's tip is fixed on the fingertip of a model hand, and the contact force F_c will occur in the orthogonal upward direction when the robot bends, as illustrated in Fig. 7(d). We collect 12 random data points from various robot configurations and hand postures, including pressures, sensor signals, and actual contact forces recorded from a 1-D force sensor (FSG005WNPB, Honeywell). To validate the force estimation algorithm, we test it in two modes: The first estimates horizontal and vertical forces without constraints, and the second incorporates constraints with prior knowledge that the contact force F_c direction is perpendicular to the tip orientation, introducing the following geometric constraint into (18):

$$f(F_x, F_y) = F_x \sin(\theta_0) + F_y \cos(\theta_0) = 0 \tag{21}$$

where the angle of the tip, θ_0, is calculated from static modeling for free motion. The functions *fminsearch* and *fmincon* in MATLAB are employed to optimize F_x and F_y without and with the geometric constraint, respectively. If no feasible solution satisfies the constraint, the best feasible point can be obtained using *fmincon*. The errors between the estimated forces $\hat{F}_x$, $\hat{F}_y$, and their resultant force $\hat{F}_c$, and the actual forces F_x, F_y, and F_c are calculated with respect to the maximum contact force. The ground truth of F_x and F_y are obtained by decomposing the force measured by the force sensor into tangential and orthogonal directions, as provided by the vision system. The comparison of the mean errors for each force range between two modes are documented in Table II. The geometric constraint reduces the errors of estimated force $\hat{F}_x$, $\hat{F}_y$ from 14.90% and 12.91% to 5.15% and 6.77%, respectively. The result also shows that the error increases as the contact force increases, and the reason is the same as in the tip load case. In terms of computational efficiency, the constraint-free force estimation algorithm averages 0.42 s per estimation, whereas the constrained algorithm averages 1.38 s per estimation. The force estimation algorithm, especially the case with constraints, introduces relatively large latency in real-time operation compared with the speed of shape reconstruction. Given that, one could potentially perform shape sensing and force estimation at different time scales. The force estimation implementation was carried out using *App Designer* in MATLAB, as shown in the online video.

VI. CONCLUSION

In this study, we present a systematic approach to simultaneous shape reconstruction and force estimation in soft bending actuators, leveraging a novel distributed inductive curvature sensor based on electromagnetic induction. In addition, a force estimation framework was proposed, facilitated by both sensor data and analytical static modeling, enabling the accurate estimation of external forces at the tip. Rigorous experiments were conducted to validate the sensor and the shape reconstruction performance, static modeling, and the force estimation algorithm.

The future work aims to use real-time shape sensing as feedback for developing control algorithms, with a focus on extending the approach to 3-D shape sensing and speeding up the force estimation algorithm.

REFERENCES

[1] R. K. Katzschmann, J. DelPreto, R. MacCurdy, and D. Rus, "Exploration of underwater life with an acoustically controlled soft robotic fish," *Sci. Robot.*, vol. 3, no. 16, 2018, Art. no. eaar3449.
[2] P. Glick, S. A. Suresh, D. Ruffatto, M. Cutkosky, M. T. Tolley, and A. Parness, "A soft robotic gripper with gecko-inspired adhesive," *IEEE Robot. Autom. Lett.*, vol. 3, no. 2, pp. 903–910, Apr. 2018.
[3] C. Hegde, J. Su, J. M. R. Tan, K. He, X. Chen, and S. Magdassi, "Sensing in soft robotics," *ACS Nano*, vol. 17, no. 16, pp. 15 277–15 307, 2023.
[4] K. Xu and N. Simaan, "An investigation of the intrinsic force sensing capabilities of continuum robots," *IEEE Trans. Robot.*, vol. 24, no. 3, pp. 576–587, Jun. 2008.
[5] P. Polygerinos et al., "Modeling of soft fiber-reinforced bending actuators," *IEEE Trans. Robot.*, vol. 31, no. 3, pp. 778–789, Jun. 2015.
[6] C. D. Santina, R. K. Katzschmann, A. Bicchi, and D. Rus, "Model-based dynamic feedback control of a planar soft robot: Trajectory tracking and interaction with the environment," *Int. J. Robot. Res.*, vol. 39, no. 4, pp. 490–513, 2020.
[7] G. Gerboni, A. Diodato, G. Ciuti, M. Cianchetti, and A. Menciassi, "Feedback control of soft robot actuators via commercial flex bend sensors," *IEEE/ASME Trans. Mechatron.*, vol. 22, no. 4, pp. 1881–1888, Aug. 2017.
[8] Z. Wang, P. Polygerinos, J. T. Overvelde, K. C. Galloway, K. Bertoldi, and C. J. Walsh, "Interaction forces of soft fiber reinforced bending actuators," *IEEE/ASME Trans. Mechatron.*, vol. 22, no. 2, pp. 717–727, Apr. 2017.
[9] R. L. Truby, C. D. Santina, and D. Rus, "Distributed proprioception of 3D configuration in soft, sensorized robots via deep learning," *IEEE Robot. Autom. Lett.*, vol. 5, no. 2, pp. 3299–3306, Apr. 2020.
[10] E. L. White, J. C. Case, and R. K. Kramer, "Multi-mode strain and curvature sensors for soft robotic applications," *Sensors Actuators A: Phys.*, vol. 253, pp. 188–197, 2017.
[11] H. Bezawada, C. Woods, and V. Vikas, "Shape reconstruction of soft manipulators using vision and IMU feedback," *IEEE Robot. Autom. Lett.*, vol. 7, no. 4, pp. 9589–9596, Oct. 2022.
[12] T. Li, L. Qiu, and H. Ren, "Distributed curvature sensing and shape reconstruction for soft manipulators with irregular cross sections based on parallel dual-FBG arrays," *IEEE/ASME Trans. Mechatron.*, vol. 25, no. 1, pp. 406–417, Feb. 2020.
[13] D. Hu, F. G.-Serchi, S. Zhang, and Y. Yang, "Stretchable e-skin and transformer enable high-resolution morphological reconstruction for soft robots," *Nat. Mach. Intell.*, vol. 5, no. 3, pp. 261–272, 2023.

[14] J. Tapia, E. Knoop, M. Mutny, M. A. Otaduy, and M. Bächer, "Makesense: Automated sensor design for proprioceptive soft robots," *Soft Robot.*, vol. 7, no. 3, pp. 332–345, 2020.
[15] F. Shahmiri and P. H. Dietz, "ShArc: A geometric technique for multi-bend/shape sensing," in *Proc. CHI Conf. Hum. Factors Comput. Syst.*, 2020, pp. 1–12.
[16] T. G. Thuruthel, B. Shih, C. Laschi, and M. T. Tolley, "Soft robot perception using embedded soft sensors and recurrent neural networks," *Sci. Robot.*, vol. 4, no. 26, 2019, Art. no. eaav1488.
[17] Y. Toshimitsu, K. W. Wong, T. Buchner, and R. Katzschmann, "SoPrA: Fabrication & dynamical modeling of a scalable soft continuum robotic arm with integrated proprioceptive sensing," in *Proc. IEEE/RSJ Int. Conf. Intell. Robots Syst.*, 2021, pp. 653–660.
[18] A. Gao, N. Liu, M. Shen, M. EMK Abdelaziz, B. Temelkuran, and G.-Z. Yang, "Laser-profiled continuum robot with integrated tension sensing for simultaneous shape and tip force estimation," *Soft Robot.*, vol. 7, no. 4, pp. 421–443, 2020.
[19] W. Felt et al., "An inductance-based sensing system for bellows-driven continuum joints in soft robots," *Auton. Robots*, vol. 43, pp. 435–448, 2019.
[20] W. Felt, M. Suen, and C. D. Remy, "Sensing the motion of bellows through changes in mutual inductance," in *Proc. IEEE/RSJ Int. Conf. Intell. Robots Syst.*, 2016, pp. 5252–5257.
[21] R. J. Webster III and B. A. Jones, "Design and kinematic modeling of constant curvature continuum robots: A review," *Int. J. Robot. Res.*, vol. 29, no. 13, pp. 1661–1683, 2010.
[22] M. H. N. Ghalati, H. Ghafarirad, A. A. Suratgar, M. Zareinejad, and M. A. A.-Pajouh, "Static modeling of soft reinforced bending actuator considering external force constraints," *Soft Robot.*, vol. 9, no. 4, pp. 776–787, 2022.
[23] S. Liu, J. Jiao, F. Meng, T. Mei, X. Sun, and W. Kong, "Modeling of a soft actuator with a semicircular cross section under gravity and external load," *IEEE Trans. Ind. Electron.*, vol. 70, no. 5, pp. 4952–4961, May 2023.
[24] Y. Mei, P. Fairchild, V. Srivastava, C. Cao, and X. Tan, "Simultaneous motion and stiffness control for soft pneumatic manipulators based on a Lagrangian-based dynamic model," in *Proc. Amer. Control Conf.*, 2023, pp. 145–152.
[25] C. Majidi, R. F. Shepherd, R. K. Kramer, G. M. Whitesides, and R. J. Wood, "Influence of surface traction on soft robot undulation," *Int. J. Robot. Res.*, vol. 32, no. 13, pp. 1577–1584, 2013.